ACS Catalysis

Research Article

pubs.acs.org/acscatalysis

Role of Coating-Metallic Support Interaction in the Properties of Electrosynthesized Rh-Based Structured Catalysts

Patricia Benito,*[,†] Wout de Nolf,*[,‡] Gert Nuyts,[‡] Marco Monti,[†] Giuseppe Fornasari,[†] Francesco Basile,[†] Koen Janssens,[‡] Francesca Ospitali,[†] Erika Scavetta,[†] Domenica Tonelli,[†] and Angelo Vaccari[†]

[†]Dipartimento di Chimica Industriale "Toso Montanari", ALMA MATER STUDIORUM -Università di Bologna, Viale Risorgimento 4, 40136 Bologna, Bologna, Italy

[‡]Department of Chemistry, University of Antwerp, Groenenborgerlaan 171, 2020 Antwerp, Antwerp, Belgium

Supporting Information

ABSTRACT: Rh-structured catalysts for the catalytic partial oxidation of CH_4 to syngas were prepared by electrosynthesis of Rh-containing hydrotalcite-type (HT) compounds on FeCrAlloy foams followed by calcination at 900 °C. During the calcination the simultaneous decomposition of the layered HT structure and formation of the protective FeCrAlloy outer shell in alumina occurred. Here, we studied the role of the coating-metallic support interaction in the properties of the catalysts after calcination, H_2 reduction, and catalytic tests, by a combination of electron (FEG-SEM/EDS) and synchrotron X-ray (XRF/XRPD and XRF/XANES) microscopic techniques. The characterization of crystalline phases in the metallic support and coating and distribution of Rh active species was carried out on several samples prepared by modifying the Rh content in the electrolytic solution (Rh/Mg/Al = 11.0/70.0/19.0, 5.0/70.0/25.0, 0/70.0/30.0 atomic ratio). A sample was also prepared with no aluminum in the electrolytic solution (Rh/Mg/Al = 13.6/86.4/0.0 atomic ratio) and calcined at 550 and 900 °C. The interaction between the elements of the metallic support and the catalytic coating increased the film adhesion during the thermal treatment and catalytic tests and modified the catalyst crystalline phases. A chemical reaction between Al coming from the foam and Mg in the coating occurred during calcination at high temperature leading to the formation of spinel phases in which rhodium is solved, together with some Rh_2O_3 and Rh^0. The metallic support was oxidized forming the corundum scale and chromium oxides, moreover ι-Al_2O_3 was identified. For the $Rh_{11.0}Mg_{70.0}Al_{19.0}$ catalyst the inclusion of Rh in the spinel phase decreased its reducibility in the H_2 pretreatment. The reduction continued during catalytic tests by feeding diluted CH_4/O_2/He gas mixtures, evidenced by the catalyst activation. While under concentrated gas mixtures the deactivation occurred, probably by oxidation.

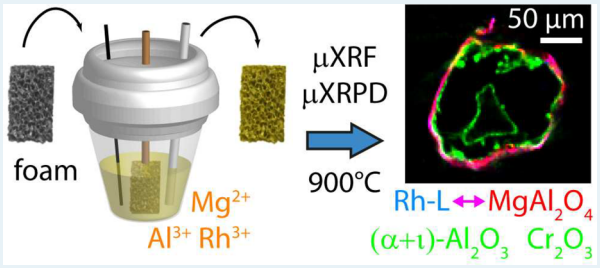

KEYWORDS: *structured catalyst, FeCrAlloy, Rh, μXRF/XRPD, μXRF/XANES, catalytic partial oxidation of CH_4*

1. INTRODUCTION

Three-dimensional ordered metallic structures (foams, fibers, honeycombs) have found application in catalytic processes for H_2 and/or syngas (CO and H_2) production,[1] such as steam reforming (SR)[2,3] and the catalytic partial oxidation (CPO)[4,5] of methane, in which heat transfer is of paramount importance. Metallic structures are coated with a catalytic film, mainly made of ceramic oxides, forming so-called structured catalysts which have great mechanical strength, large geometric surface area, low pressure drop, and enhanced heat conductivity.[6−8] In the past, some of us have already proposed the coating of FeCrAlloy foams with layered hydrotalcite-type (HT) compounds by electrosynthesis to prepare Rh-containing catalysts active in the CPO of CH_4,[9,10] as an alternative to the conventional washcoating procedure.[11] Electrosynthesis makes it possible to coat metallic foams with small pores by applying a cathodic potential for short times to a metallic foam immersed in a solution containing the nitrates of the cations to be deposited. The film adheres well to the metallic support, and its composition and thickness depend on the potential applied, synthesis time, and composition of the electrolytic solution. The CPO of CH_4 achieves high conversion and selectivity in CO and H_2 (H_2/CO = 2/1) at very short contact times;[12,13] nevertheless, hot spots and a large pressure drop may be generated, entailing safety risks in the operation. Structured catalysts based on thermally conductive metallic supports help to keep CPO drawbacks under control. However, the metallic support may be altered under preparation and harsh reaction conditions.

In fact, one of the main issues concerning the application of metallic structured catalysts is the oxidation or corrosion of the metallic material such as Al, Cu, AISI 314 (American Iron and Steel Institute) stainless steel, and FeCrAlloy. Usually the metal is pretreated to create a protective oxide outer shell as well as to

Received: March 24, 2014
Revised: September 5, 2014
Published: September 11, 2014

 © 2014 American Chemical Society dx.doi.org/10.1021/cs501079k | ACS Catal. 2014, 4, 3779−3790

increase its adherence to the catalyst.[8,14] The most common alloy used in high-temperature applications is FeCrAlloy, even though its thermal conductivity is not very high.[7] The oxidation of the main elements of the support, Fe and Cr, is prevented by the formation of a protective alumina scale;[15] Y, also present in the alloy, is localized in spots forming Y−Fe intermetallic compounds precipitated at the grain boundaries which, after calcination in air, form $Y_3Al_5O_{12}$.[16] Alumina scale properties are determined by calcination temperature,[17] heating[18] and cooling rate,[19] oxygen concentration,[17] and environment,[20] and they can be modified either by thermal cycling conditions[21] or after a long operation time.[22]

Another issue to take into account when dealing with metallic supports is the fact that the interaction between the elements of the metallic support and the catalytic coating may modify the activity (poisoning or activation) as well as the properties of the protective outer shell, such as its thickness and adhesion to the substrate.[23−25] Few articles dealing with FeCrAlloy supports report the migration of alloy elements into coatings made by ZSM-5 zeolite,[26] Au/TiO_2,[27] Au/CeO_2,[28] and CuO_x/CeO_2.[29]

In electrosynthesized catalysts the metallic support interaction may play an important role in the properties of the final catalysts. During electrosynthesis, Rh/Mg/Al HT precursors are precipitated on the surface of the support and calcination at 900 °C is required to obtain the actual catalyst. The decomposition of the HT structure and the formation of the protective alumina scale take place simultaneously during calcination. Thus, a chemical reaction between the elements from foam and coating may also occur. This may modify the phases present in the catalyst after HT decomposition−namely the ratio between MgO and $MgAl_2O_4$-type phases in which Rh species are included−and, as a result, the properties of metallic particles and catalytic performances.[30,31] In order to study these aspects, a structural characterization of the alumina outer oxide shell and coating as well as the speciation of the Rh active phase in electrosynthesized catalysts is necessary. However, these are not simple issues, because of (i) the formation of films of a thickness of few μm and (ii) the complex shape of the foam supports.

Most of the structured catalyst characterization was performed by SEM coupled with elemental analysis (EDS or EPMA),[26] FIB/STEM,[32] and GD-OES.[27] Conventional XRPD was used to characterize crystalline phases mostly in films coating planar materials.[27] However, when dealing with complex shaped supports, such as foams, the materials are usually modified to perform measurements,[33] and the spatial distribution of crystalline phases in coatings cannot be studied. In a previous work we had shown the potential of synchrotron-based microscopic techniques such as μXRF/XRPD to study "as prepared" Ni-structured catalysts consisting of FeCrAlloy foams coated with a thin catalytic film.[34]

The high brilliance at synchrotron beamlines makes it possible to obtain elemental (μXRF) and crystalline phase distribution maps (μXRPD) with micrometer or submicrometer resolution and high sensitivity. These combined techniques have found application in the characterization of pigments and paintings[35] and catalysts.[36−40] Similarly, μXANES[39,41−43] can be used to determinate the oxidation state and chemical environment of active Rh species in the coating. XANES is a powerful technique for the study of Rh-based catalysts,[44] and studies under CPO working conditions[45−47] have evidenced changes in the Rh oxidation state (from Rh^{3+} to active Rh^0) during catalytic tests. Given the coating dimensions (1−10 μm), a microbeam is necessary to examine the Rh speciation across this thin film. In addition to the beam size, the escape distance of X-rays detected from the material should be of the same order of magnitude as the sample thickness, otherwise the signal is averaged in depth, leading to a degradation of the spatial resolution.[48] Thus, instead of measuring the absorption fine structure around the Rh−K edge;[44,45] the less energetic Rh-L3 edge[49−51] can be measured to study Rh-containing species. In this way, the penetration depth of the radiation is of the same order of magnitude as the thickness of the coating, and only Rh-containing species at the surface of the film of foam strut cross-section coatings are studied.

In this paper, to study the role of the coating-metallic support interaction in electrosynthesized Rh-based structured catalysts, Rh/Mg/Al HTs are synthesized on FeCrAlloy foams and characterized after calcination, H_2 reduction, and CPO of CH_4 tests[10] by a combination of electron microscopy techniques, μXRF/XRPD (as previously reported by us), and, for the first time, also by μXANES. The amount of Mg^{2+}, Rh^{3+}, and/or Al^{3+} in the electrolytic solution (Rh/Mg/Al = 11.0/70.0/19.0, 5.0/70.0/25.0, 0/70.0/30.0, 13.6/86.4/0 atomic ratio) and the calcination temperature (550 and 900 °C) are varied to study at the different steps of catalyst life cycle: (i) catalytic coating features, such as crystalline phases, Rh distribution, oxidation state, and catalytic activity, (ii) the formation of protective Al_2O_3 scale, and (iii) crystalline phases in the metallic support.

2. EXPERIMENTAL SECTION

2.1. Electrosynthesis. Electrosyntheses were performed in a single-compartment three-electrode cell at −1.2 V vs SCE for 2000 s as reported previously.[10] FeCrAlloy foam cylinders (60 ppi and 10.0 × 11.9 mm) were the working electrodes. An aqueous solution containing KNO_3 as the supporting electrolyte (0.3 M) and the salts of the cations to be deposited − $Mg(NO_3)_2$, $Al(NO_3)_3$, and $Rh(NO_3)_3$ (0.03 M) − were used as the electrolytic solution. Different Rh/Mg/Al atomic ratios were studied: 11.0/70.0/19.0, 5.0/70.0/25.0, 0/70.0/30.0, 13.6/86.4/0.

2.2. Characterization Techniques. SEM/EDS analyses were performed by using an EVO 50 Series Instrument (LEO ZEISS) equipped with an INCAEnergy 350 EDS micro analysis system and an INCASmartMap for the imaging of the spatial variation of elements in a sample (Oxford Instruments Analytical). The accelerating voltage was 20 kV, and the spectra collection time was 60 s. FEG-SEM/EDS analyses were performed with a (FESEM) Zeiss SUPRA40VP coupled with an EDS system with a high surface detector X-Max 50 mm. Temperature-Programmed Reduction (TPR) analyses were carried out by feeding a H_2/Ar gas mixture (5/95 v/v, total flow 20 mL/min) in the 60−950 °C range using ThermoQuest CE Instruments TPDRO 1100.

For the tomographic experiments, samples were prepared by isolating individual struts from the support foams and gluing them to the top of glass capillaries, while enabling an easy rotation in the beam. Combined micro X-ray Fluorescence (μXRF) and micro X-ray Powder Diffraction (μXRPD) measurements in both 2D scanning and tomographic mode were performed at the MicroXAS beamline of the Swiss Light Source (Paul Scherrer Institute, Villigen, CH).[52] The polychromatic beam from the undulator source was monochromatized to 18 keV using a Si(111) double crystal monochromator and subsequently focused on the sample by

dx.doi.org/10.1021/cs501079k | ACS Catal. 2014, 4, 3779−3790

means of a Kirkpatrick-Baez mirror system, thus achieving a spot size of 1.5 × 3.0 μm (h × v). Two single-element silicon drift detectors (KETEK GmbH, D) collected the fluorescent radiation produced by the irradiated specimen under 90° from the incoming X-rays. A He flight path was used between the sample and the XRF detectors in order to reduce the air absorption of low energy fluorescence signals such as Rh-L_α (2.697 keV), Al-K_α (1.486 keV), and Mg-K_α (1.254 keV). A Pilatus 100 K detector (DECTRIS, CH, pixel size 172 μm) positioned behind the sample was used to register the Debye rings produced by the interference of the X-ray photons elastically scattered by the sample.

For the scanning experiments, the sample was translated in a plane perpendicular to the primary X-ray beam, with a step size equal to the beam size. During tomographic measurements, the sample was moved horizontally with the same step size as in the 2D scanning experiments and was rotated over 180°.

The information extracted from the scanning and the tomography measurements is of the same nature, namely two-dimensional distribution maps of the elemental (XRF) and crystalline phase (XRPD) composition. In the 2D scanning mode, these maps represent the projection of 3D elemental and phase distributions on a vertical YZ-plane perpendicular to the primary X-ray beam. In the tomographic mode, projections were collected at a specific height Z and under different angles ω to obtain (Yω)-distribution maps, called sinograms. On the basis of the latter, the distributions in a virtual, horizontal XY-plane through the sample can be calculated. The iterative MLEM (Maximum Likelihood Expectation Maximization) algorithm was used for this purpose, since it features a superior reconstruction quality over the FBP-method (Filtered Back-projection) in the presence of artifacts. More details can be found elsewhere.[53−55] To construct the X-ray fluorescence (YZ) or (Yω)-maps, the net elemental line intensities were obtained by the least-squares fitting of raw XRF spectra.[56] For X-ray Powder Diffraction maps, Rietveld refinement was performed with fixed relative peak intensities (i.e., fixed atomic parameters). The only remaining refinable parameters, after determining the XRPD line shapes, were the scaling factors of each crystallographic phase included in the fitting model, their unit cell parameters, and the sample−detector distance. The scaling factors are proportional to the abundance of the specific compounds present and, therefore, are suitable for visualizing phase distributions.[57]

XANES profiles of Rh reference compounds at the Rh-L3 edge were collected at the European Synchrotron Radiation Facility (ESRF, Grenoble, F), on beamline ID21. The storage ring operating conditions were 6 GeV electron energy with 200 mA electron current and 7/8 multibunch operating mode. For these experiments a Si(111) double-crystal monochromator with an energy resolution of 10^{-4} ($\Delta E/E$) was used. A metallic Rh reference foil (0.75 μm) was used to provide an accurate energy calibration for all the spectra (first inflection point of the Rh-L_3 edge set at 3004 eV).[58] The two monochromator crystals were detuned slightly to remove the high-energy harmonics from the incident X-ray beam.

In order to limit self-absorption, the appropriate amounts of Rh model compounds were mixed with boron nitride, resulting in a weight percentage equal to 2% of the model compound. Each mixture was compressed into a pellet and placed in a sample holder. In order to avoid contributions of possible heterogeneities during mixing, measurements were performed with an unfocused beam using a 200 μm pinhole. When needed (low Rh content in pellet), the pinhole was removed, resulting in a beam size of ∼500 μm^2. XANES spectra were recorded with the sample positioned at 45° with respect to the incoming beam. The fluorescence was recorded as a function of the X-ray energy using a photodiode and a silicon drift diode (Bruker) (depending on the count rate) at an angle of 45° to the sample. XANES spectra were collected from ∼35 eV below to ∼130 eV above the Rh-L_3 edge (2970 eV−3135 eV), with 0.25 eV steps for the entire measured region. A 100 ms integration time was used for each energy, resulting in a measuring time of ∼1 min per XANES spectrum. Twenty repeats were recorded for each Rh model compound to reduce noise.

On the Rh-based catalysts, measurements were performed at the Swiss Light Source (SLS, PSI, Villigen, CH), on the Phoenix end station. The storage ring operating conditions were 2.4 GeV electron energy with 400 mA electron current. A monochromator similar to the one at beamline ID21 was used. Also, the angles of the incoming X-ray beam and the detected XRF signal in relation to the sample surface were the same as described for the measurement of the Rh model compounds. Here the beam size was reduced to approximately 5.5 × 5.5 μm^2 with a Kirkpatrick-Baez mirror system. Foam cylinders were embedded in a resin (Technovit 4006, Heraus Kulzer) and cut; then the polished cross sections of the struts were analyzed. The thickness of the embedded samples prevented transmission measurements, thus making possible only the monitoring of the fluorescence intensity as a function of the excitation energy. For this purpose, a 4-element SDD detector (Vortex) was used. XANES spectra were collected from ∼85 eV below to ∼130 eV above the Rh-L_3 edge (2920 eV−3135 eV).

For all the XANES spectra, normalization was performed using the ATHENA software package. An edge-step normalization was performed by linear pre-edge subtraction and by the regression of a (in general) quadratic polynomial beyond the edge.[59] If a silicon drift detector was used for the collection of XANES spectra, the recorded XRF spectra were evaluated using the PyMCA software package. Then the fitted Rh intensity (sum of all Rh-L lines) was plotted as a function of the excitation energy, resulting in a (fluorescence mode) XANES spectrum.

μXRF maps were also collected at the Phoenix Beamline using the same setup and using an SDD detector as described in the measurements of actual Rh-based catalysts (spot size of 5.5 × 5.5 μm^2) with a step size of 5 μm. A primary excitation energy of 3006.25 eV (white line of Rh spinel) was used to obtain a maximum Rh fluorescence intensity. These maps were used to detect interesting spots within the Rh layer in which XANES spectra were recorded. All maps were recorded with an exposure time of 1 s per pixel.

2.3. Catalytic Tests. CPO tests were carried out in a quartz reactor (i.d. 10.0 mm) operating at atmospheric pressure as reported elsewhere.[10] Two foam cylinders (10.0 × 11.9 mm) coated with $Rh_{11.0}Mg_{70.0}Al_{19.0}$ compounds were loaded in the isothermal zone of the reactor. Before tests, catalysts were reduced *in situ* by an equimolar H_2/N_2 mixture (7.0 L/h) for 2 h at 750 °C, then the feed was switched to the CH_4/O_2/He gas mixture, and the oven temperature was set at 750 °C. Different GHSV values and gas mixture compositions were used: GHSV = 11,500, 15,250, 38,700, and 63,300 h^{-1} (referring to the total volume of the foam support at STP conditions) and CH_4/O_2/He = 2/1/20 and 2/1/4 (v/v). Reaction products were analyzed online after H_2O condensation using a PerkinElmer Autosystem XL gas chromatograph, equipped with two thermal

dx.doi.org/10.1021/cs501079k | ACS Catal. 2014, 4, 3779−3790

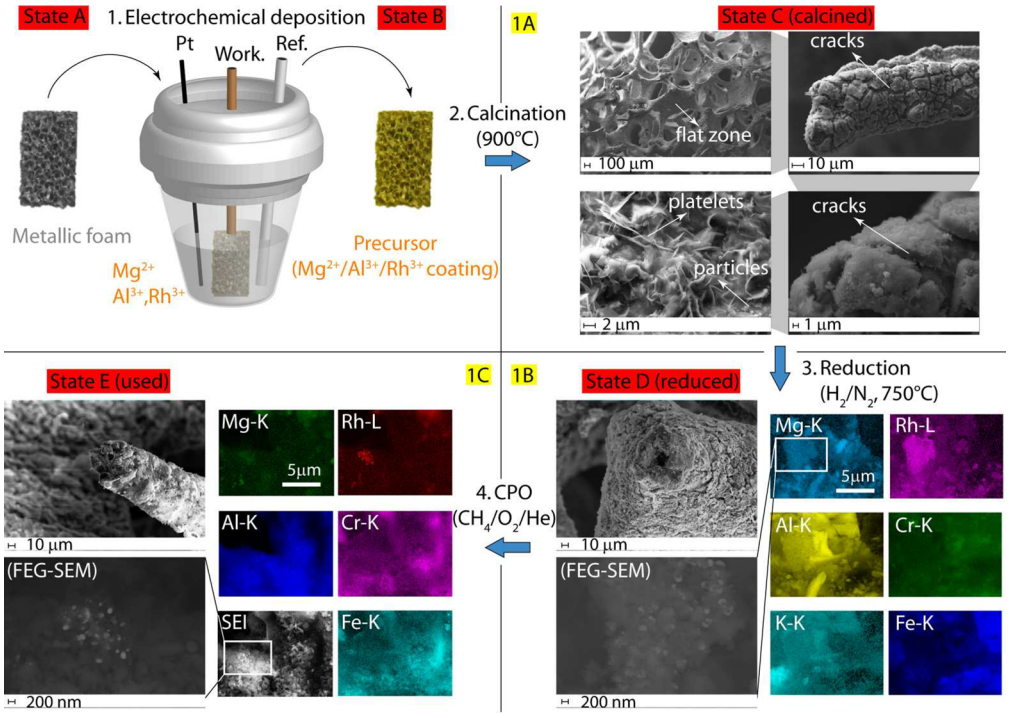

Figure 1. Life cycle of a Rh-coated structured catalyst. 1A) Secondary electron images of state C made the morphological studies of the coating possible. 1B and 1C) High resolution EDS maps visualized elemental distributions in state D and state E; FEG-SEM backscattered electron images permitted an estimation of Rh particle sizes.

conductivity detectors (TCD) and two Carbosphere columns, with He as the carrier gas for the CH_4, O_2, CO, and CO_2 analyses and N_2 for the H_2 analysis.

3. RESULTS AND DISCUSSION

The life cycle of Rh-coated structured catalysts is broken down into several stages as summarized in Figure 1 and Table 1. Rh/Mg/Al HT compounds (state B) were precipitated on the surface of the support (state A) by the electrobase generation method under selected synthesis conditions, i.e. −1.2 V vs SCE and 2000 s,[10] and using electrolytic solutions with different Rh/Mg/Al atomic ratios. Catalysts (in state C) are obtained by calcination at 900 °C in static air. The $Rh_{11.0}Mg_{70.0}Al_{19.0}$ catalyst, after activation (state D) with an equimolar H_2/N_2 mixture, was tested in the CPO of CH_4 to evidence possible alterations in the properties of the coating and support (state E).[10]

Table 1. Life Cycle States of an Electrosynthesized Catalyst

state	description
A	bare foam
B	electrosynthesis
C	calcination at 900 °C for 12 h
D	reduction H_2/N_2 1:1 v/v, 750 °C for 2 h
E	CPO catalytic tests

3.1. Characterization of Catalysts. *Characterization by SEM/EDS.* Regardless of the electrolytic solution composition, the catalyst layer appeared to be well-anchored to the support, although uncoated support struts were found in some parts of the foam (mainly in flat areas; Figure 1A). Furthermore, the morphology of the coating did not appear to depend on the composition of the electrolytic solution. The coating was made of agglomerates of small particles or platelets, forming a 2−3 μm-thick layer with visible cracks (Figure 1A). The Mg/Rh ratio in the particle agglomerates, obtained through EDS analysis, was lower than the value in the electrolytic solution (approximately 3−4 vs 6.35), whereas the opposite is true for platelets (approximately 10).[10] Furthermore, it was observed that some potassium from the electrolytic solution was also deposited on the foam surface and that the concentration of Cr increased in some areas.

FEG-SEM images of the $Rh_{11.0}Mg_{70.0}Al_{19.0}$ sample after reduction (state D) were taken in order to study the particle size of Rh^0 particles. High-resolution backscattering FEG-SEM images (Figure 1B) indicated the formation of Rh-containing particles with a broad particle size distribution, from 60 to 280 nm, probably due to the high Rh loading in the catalysts.

High-resolution EDS maps (Figure 1B) produced interesting qualitative information on the spatial distribution of the elements from both the coating and the support. Among the deposited elements, Rh and Mg distribution corresponded to a large extent, while the correlation with Al was observed in some areas only. This behavior may be explained considering that Al is also a constituent of the foam alloy, thus its distribution in the alloy and the film thickness may affect the correlation. Lastly, Fe and Cr (the major foam alloy constituents) distribution was not always correlated; Cr was more concentrated in some areas, indicating the presence of Cr_2O_3. The presence of chromium oxides may promote the total oxidation of CH_4.[60]

Speciation by Means of μXRF/XRPD. The distribution of elements and crystalline phases in virtual cross sections of individual foam struts were obtained by combined μXRF/XRPD tomography for all the catalysts. The results obtained for the calcined $Rh_{11.0}Mg_{70.0}Al_{19.0}$ sample (state C) are shown in Figure 2 and Figure S1. An Fe/Cr alloy and a τ-carbide

dx.doi.org/10.1021/cs501079k | ACS Catal. 2014, 4, 3779−3790

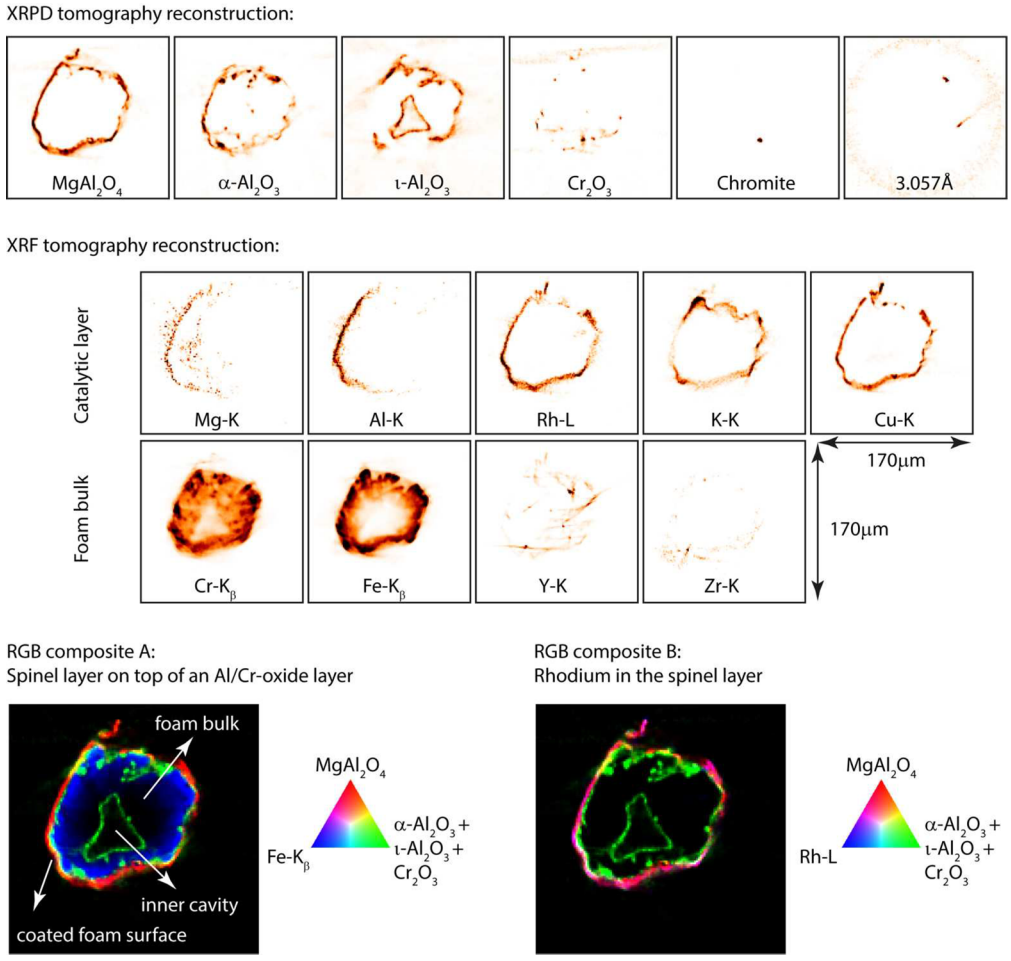

Figure 2. Elemental and crystalline distributions in a virtual cross-section of a calcined $Rh_{11.0}Mg_{70.0}Al_{19.0}$ strut (state C). Translation: 170 μm (1.3 μm steps); Rotation: 180° (1° steps); Time: 1 s per point. Elemental maps were constructed from the intensity of emission line groups K_α, K, or L. The apparent absence of Mg and Al on the right side of the images may be attributed to the failure of the He flux in front of one of the XRF detectors. Fe and Cr suffered from self-absorption. Compound maps were constructed from Rietveld scaling factors. RGB composite maps showed that, roughly, two layers were formed on top of the foam surface: a spinel layer (containing Rh) and an Al/Cr-oxide layer.

($Cr_{23+x}Fe_xC_6$) were identified in the foam bulk material (Figure S1). The latter may be related to carbon impurities in the foam raw material, which was observed to segregate together with Cr at the alloy grain boundaries during heating.[61,62] Poor grain statistics of the two substrate phases did not permit reliable tomographic reconstruction of the corresponding XRPD signals, and therefore Fe fluorescence was used to visualize the location of the substrate surface for other phases. Alongside the major constituents, Fe and Cr, hot spots of Y and Zr were observed in the foam material.

Mg, Al, and Rh ions from the electrolytic solution were localized on top of the substrate (state C), covering approximately the entire circumference of the foam strut (Figure 2). The Mg-containing phase was identified as $MgAl_2O_4$ (spinel). Surprisingly, MgO, obtained by calcination of HT compounds under similar conditions,[31] was not identified. Here it should be pointed out that the formation of amorphous MgO may be ruled out, considering the high calcination temperatures; as reported above, MgO was always observed on coprecipitated HT compounds with a Mg/Al atomic ratio >1/2 and calcined at 900 °C.[31] Moreover, the distributions of the Mg XRF signal and $MgAl_2O_4$ XRPD signal were well correlated, thus suggesting that most of the Mg was in the spinel phase. Alongside $MgAl_2O_4$, the Al-containing phases α-Al_2O_3 and ι-Al_2O_3 were also present. The latter was originally identified as a metastable phase in the cryolite-alumina phase diagram,[63] with a crystal structure almost indistinguishable from $K_{2/3}Al_6O_{10-2/3}$ (K-mullite).[64,65] Although potassium was found in the substrate coating, the comparison between the K and ι-Al_2O_3 distributions did not provide convincing evidence of the inclusion of K^+ cations in this structure. Keeping this in mind, we will refer to this phase as ι-Al_2O_3 later in this article, even though it cannot be explained how a metastable phase may be sustained without quenching. Note also that, in Figure 2, the ι-Al_2O_3 distribution map shows a second layer inside the foam strut. The metallic foam struts may contain cavities which are connected to the outside, thereby allowing coating of the inner cavities as well as the outer surface of the foam.[34]

The α-Al_2O_3 phase, which is intended to form a protective outer shell against substrate corrosion, did not completely cover the foam surface. Moreover, corrosion products such as Cr_2O_3 and $FeCr_2O_4$ (chromite) were observed as hot spots, in agreement with EDS results that indicated a Cr enrichment in some areas. As can be seen in Figure 2, the spinel layer formed on top of the alumina layer (comprising α- and ι-Al_2O_3) and the latter contained Cr_2O_3 in some parts. On average, these

dx.doi.org/10.1021/cs501079k | ACS Catal. 2014, 4, 3779−3790

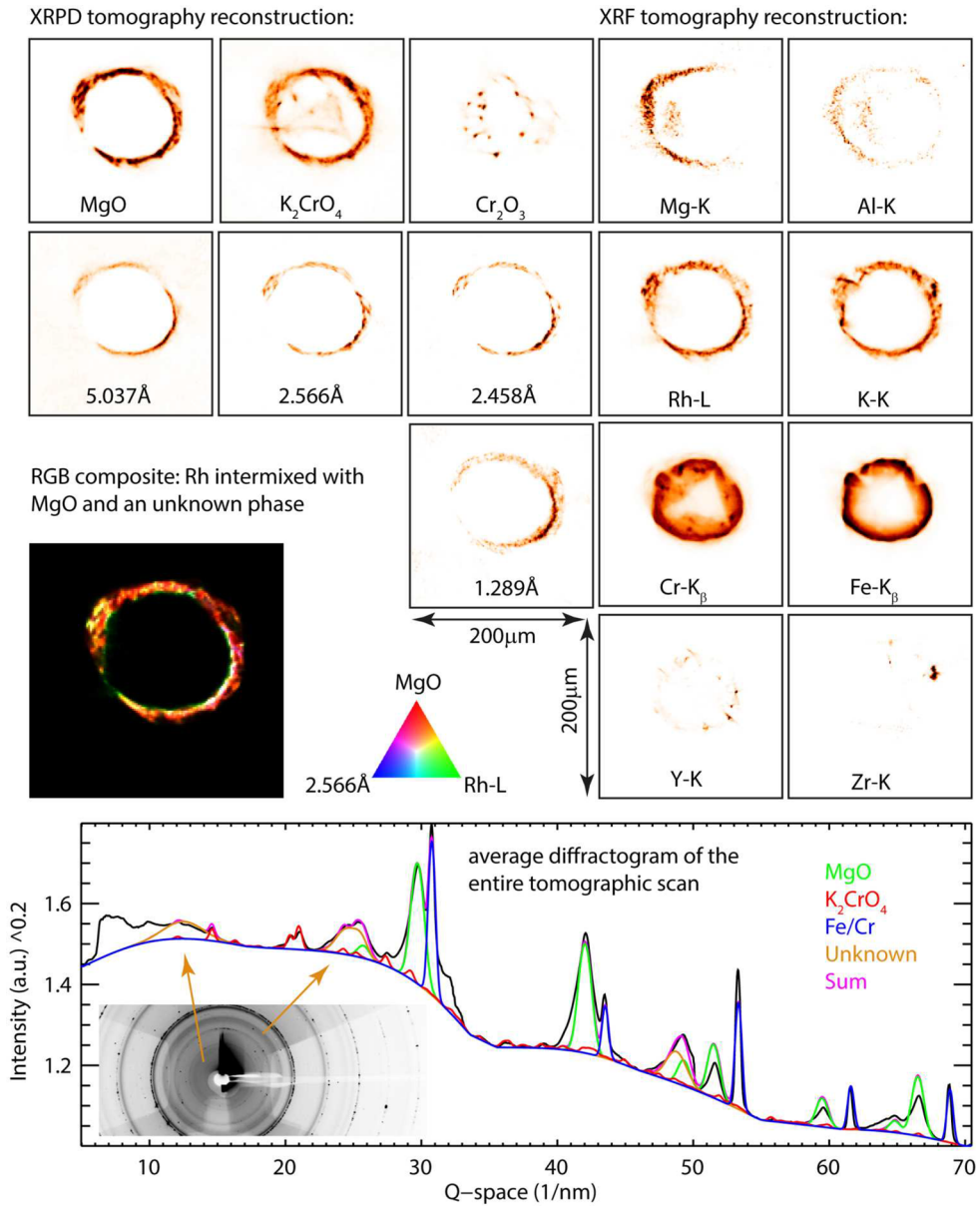

Figure 3. Elemental and crystalline distributions in a virtual cross-section of calcined $Rh_{13.6}Mg_{86.4}$ at 550 °C. Translation: 200 μm (1.5 μm steps); Rotation: 180° (1.2° steps); Time: 1 s per point. Only one layer on the foam surface was observed, containing MgO, K_2CrO_4, and rhodium. Additionally, an unidentified nanocrystalline phase (broad Bragg peaks) was present.

layers were not thicker than the beam size used for the investigation, i.e. 1.5 μm.

Lastly, no Rh-containing phase was identified, although a distinct correlation could be observed between the elemental Rh map and $MgAl_2O_4$ distribution, suggesting that Rh^{3+} may partially substitute Al^{3+} cations in the spinel structure. The absence of the Rh-containing phase may be due to the fact that low degrees of substitution are not distinguishable from no substitution at all (i.e., $MgAl_2O_4$), as the difference in Bragg peak positions and relative intensities are negligible (see below the characterization of $Rh_{13.6}Mg_{86.4}$). The same observation could be true for Cu, which might come from a Cu wire used in the electrochemical cell. No crystalline phase containing Cu was identified, although it may be present in the $MgAl_2O_4$ phase.

The calcined samples prepared with less or no Rh content in the electrolytic solution ($Rh_{5.0}Mg_{70.0}Al_{25.0}$ in Figure S2 and $Mg_{70.0}Al_{30.0}$ in Figure S3) proved to have a composition comparable to the $Rh_{11.0}Mg_{70.0}Al_{19.0}$ sample. This behavior confirms that Rh and the Al content in the solution do not alter the main crystalline phases. Mg, Al, and Rh (when present) were well distributed on the foam surface. The main crystalline phase in the coating was $MgAl_2O_4$, and no Rh-containing phases were identified in $Rh_{5.0}Mg_{70.0}Al_{25.0}$, but Rh was well correlated to the spinel phase. There were, however, several unidentified signals in the XRPD data that might be attributed to γ-Al_2O_3 (a defect spinel structure[66]). Moreover, the aluminum oxide layer on the outer surface of the $Rh_{5.0}Mg_{70.0}Al_{25.0}$ sample was made of γ-Al_2O_3, while the oxides, also observed in the $Rh_{11.0}Mg_{70.0}Al_{19.0}$ sample (α-Al_2O_3, ι-Al_2O_3 and Cr_2O_3), were mostly present on the inner cavity surface.

In summary, the catalyst characterization by means of μXRF/XRPD confirmed that the Al_2O_3 protective scale does not properly coat the foam surface, and it appeared that the metallic

dx.doi.org/10.1021/cs501079k | ACS Catal. 2014, 4, 3779−3790

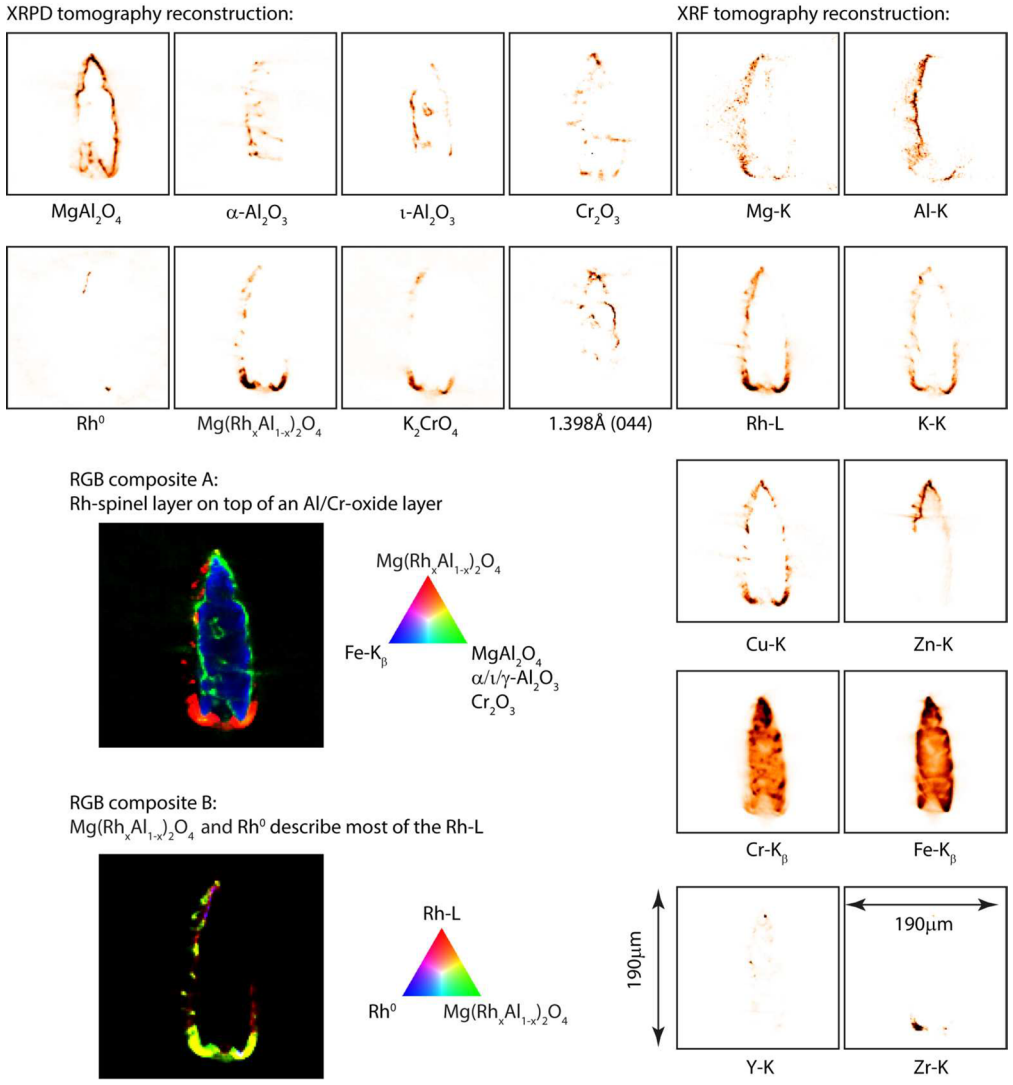

Figure 4. Elemental and crystalline distributions in a virtual cross-section of $Rh_{13.6}Mg_{86.4}$ calcined at 900 °C (state C). Translation: 190 μm (1.5 μm steps); Rotation: 180° (1.2° steps); Time: 1 s per point. The unidentified 1.397 Å Bragg peak may be attributed to the most intense reflection (044) of γ-Al_2O_3 (having a defect spinel structure[66]). RGB composite maps showed that an oxidized layer covered the foam surface ($MgAl_2O_4$, $\alpha/\iota/\gamma$-Al_2O_3, and Cr_2O_3). Less tightly covering the surface rhodium containing phases $Mg(Rh_xAl_{1-x})_2O_4$ and Rh^0 were found, including Cu and K contamination, the latter as K_2CrO_4.

material was altered and formed chromium oxides. Moreover, the coating is mainly made of spinel phase, and no MgO was identified. The absence of MgO and the changes in the formation of the corundum scale may be related to (i) the composition of the deposited coating, (ii) an interaction between the coating and foam elements, or (iii) a combination of both effects. As previously reported by EDS spectra, the composition of the deposited film differs from that of the electrolytic solution. If a solid with an Al content larger than expected is deposited, the Mg/Al ratio will change, and therefore the ratio between the expected MgO and $MgAl_2O_4$ phases obtained after calcination will also. On the other hand, the solid state reaction between oxidized Al from the foam and Mg from the coating during calcination might contribute to the formation of $MgAl_2O_4$ rather than of MgO and protective corundum scale. In fact, although in the final catalyst the alumina is the α-Al_2O_3, more reactive alumina polymorphs are obtained first.[67]

In order to discriminate between the contribution of Al from the deposited coating or from the foam to the formation of the spinel phase, a catalyst was prepared with no Al^{3+} cations in the electrolytic solution (i.e., $Rh_{13.6}Mg_{86.4}$). Moreover, to gain more insight into the order of formation of different compounds in both the coating and the metallic support during calcination, the $Rh_{13.6}Mg_{86.4}$ sample was calcined at 550 and 900 °C. At 550 °C the HT layered structure collapsed, forming mixed oxides; however, this temperature was significantly lower than the value required for the formation of spinels and the protective corundum shell.[31,67]

μXRF/XRPD results of $Rh_{13.6}Mg_{86.4}$ sample after calcination at 550 °C are displayed in Figure 3. The electrodeposited Mg and Rh elements coat the strut surface rather homogeneously, with the exception of a small area. Moreover, the K layer may be clearly distinguished. The FeCrAlloy corrosion product is composed not only of Cr_2O_3, as observed in previous samples, but also of K_2CrO_4. Cr_2O_3 was also present as hot spots, whereas a K_2CrO_4 layer could be observed on the strut surface. Thus, it follows that foam oxidation occurred before the formation of the protective alumina shell. The oxidation of chromium may be fostered by the reaction of Cr_2O_3 with the

dx.doi.org/10.1021/cs501079k | ACS Catal. 2014, 4, 3779−3790

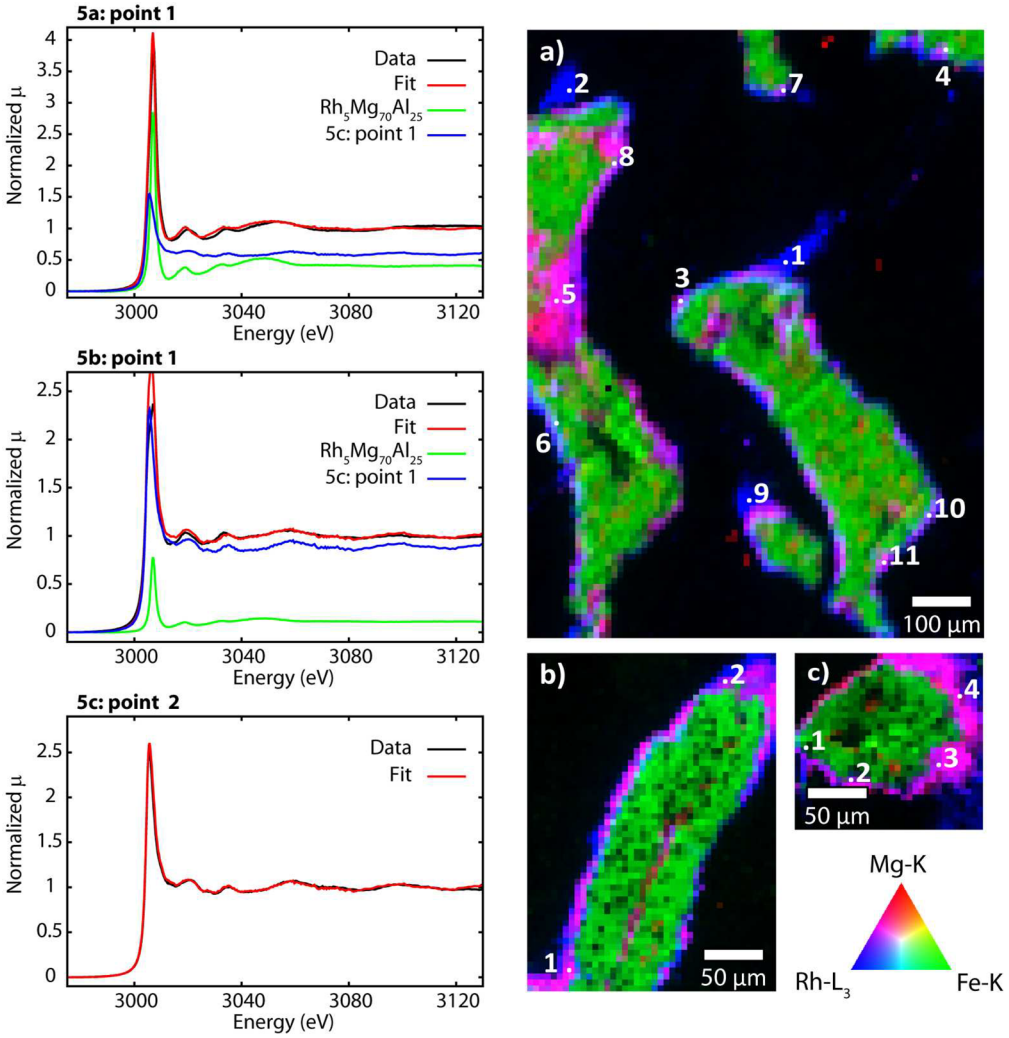

Figure 5. RGB composite maps of a cross-section of $Rh_{11.0}Mg_{70.0}Al_{19.0}$ struts in state C (a), D (b), and E (c). The numbers given mark the spots where XANES measurements were performed; an example of the result of a linear combination fit is given for each state.

electrodeposited K, forming K_2CrO_4.[68−70] The absence of FeCrAlloy corrosion products in calcined bare foam (i.e., calcined without deposited material, see Figure S5) supports the hypothesis that K is involved in the foam oxidation. However, the change in the material during the application of the cathodic potential may not be ruled out. Lastly, it must be noted that K distribution is correlated with that of K_2CrO_4 (see Figure 3), thereby adding evidence of the presence of ι-Al_2O_3 over K-mullite.

The MgO phase was observed by XRPD together with another unidentified nanocrystalline phase (Figure 3). The formation of crystalline MgO at low temperature calcination is further evidence against the presence of amorphous MgO in the catalyst calcined at 900 °C; if MgO is crystalline at 550 °C, an increase in the calcination temperature will only enhance its crystallinity. The exact speciation of Rh after calcination at 550 °C remains unclear, although it appears to be correlated with MgO and probably in parts with the unidentified phase. Similarly to $MgAl_2O_4$, Rh cations may be included in the MgO structure, which may be described as a spinel superstructure.[71]

After calcination at 900 °C of the $Rh_{13.6}Mg_{86.4}$ sample (state C), the following Al-containing phases already observed in the catalyst with added Al ($Rh_{11.0}Mg_{70.0}Al_{19.0}$) were also identified: $MgAl_2O_4$, α-Al_2O_3, and ι-Al_2O_3 (Figure 4). Chromium oxides, Cr_2O_3 and K_2CrO_4, were still identified, but potassium chromate only formed some spots, not a layer. The decrease in the K_2CrO_4 phase may be related to its thermal decomposition. Corundum was present in some parts of the surface, whereas $MgAl_2O_4$ and K-mullite seemed to be mutually exclusive, thus suggesting that the formation of the latter phases inhibits the formation of the corundum scale.

A detailed Rietveld analysis of the patterns was performed. The spinel structure was described as reported by Andreozzi et al.[72] with zero inversion. Within this "normal" spinel structure, the degree of Rh^{3+} substitution on the Al^{3+} site (octahedral 16d) derives from the fitted unit cell parameter using the empirical relation composed by Capobianco.[73] The direct fitting of the site occupation factors is not reliable for microdiffraction since relative peak intensities deviate from their values for an ideal powder due to the lack of crystal orientations present in a micron beam. The Rietveld refinement revealed that the coating was actually made of two magnesium-containing spinel phases: $MgAl_2O_4$ and $Mg(Rh_xAl_{1-x})_2O_4$. A clear distinction could be observed (see Figure S4) between the spinel with significant Rh substitution [corresponding to $Mg(Rh_xAl_{1-x})_2O_4$ with $x \approx 0.7$] and the one with little or no Rh substitution ($MgAl_2O_4$). From the correlation with the Rh distribution, however, it appears that all Rh was present in the

dx.doi.org/10.1021/cs501079k | ACS Catal. 2014, 4, 3779−3790

$Mg(Rh_xAl_{1-x})_2O_4$ phase, apart from metallic rhodium (Rh^0) that was formed in some spots, despite the oxidizing conditions during calcination (see Figure 4).

These results demonstrate that Al−Rh substitution may occur in the spinel structure obtained after calcination. Therefore, it is plausible that in the $Rh_{11.0}Mg_{70.0}Al_{19.0}$ catalyst discussed above (see Figure 2), some substitution also took place; however, a low degree of substitution was not distinguishable by XRPD. The presence of Rh in the spinel phase is supported by the Temperature-Programmed Reduction (TPR) performed on this catalyst, allowing the characterization of a full foam cylinder.[10] H_2 consumption peaks were attributed to Rh_2O_3 and Rh species reduced at higher temperature in oxides, which were obtained by calcination of the HT phase. However, the Rh_2O_3 species could not be identified in the recorded XRPD data, suggesting that either their concentration was too low to be detected, or they were not crystalline.

As can be seen in Figure 4, in the $Rh_{13.6}Mg_{86.4}$ sample the Rh-containing phases (Rh^0 and $Mg(Rh_xAl_{1-x})_2O_4$) seem to form a thicker layer on top of a thinner alumina layer (α-Al_2O_3, ι-Al_2O_3, and probably γ-Al_2O_3). Conversely to what was observed in calcined foams with added Al (e.g., $Rh_{11.0}Mg_{70.0}Al_{19.0}$ in Figure 2), $MgAl_2O_4$ completed the alumina layer in the parts where it is interrupted. The only source of Al in the $Rh_{13.6}Mg_{86.4}$ catalyst was the FeCrAlloy substrate material. Thus, it may be concluded that Al migrated from the FeCrAlloy to form spinel and Al oxides during calcination. The interdiffusion between the coating and the substrate elements forming the spinel phase may have a dual effect. On the one hand, it may enhance the anchoring between the catalyst and the metallic substrate, passing from a mechanical[74] to a chemical interaction, since the coating may be considered as becoming an integral part of the substrate material.[75] On the other hand, the formation of the corundum protective scale decreased. Lastly, it should be considered that the differences in porosity related to the formation of the spinel instead of the alumina scale alter the rate of diffusion of ions in the FeCrAlloy and therefore its oxidation rate.

Speciation by Means of μXRF/XANES. Even when employing the full Rietveld refinement of diffraction patterns, some limitations were found in determining the exact location of Rh active species in the catalytic coating. More detailed information about the distribution of Rh in two samples, $Rh_{11.0}Mg_{70.0}Al_{19.0}$ and $Rh_{13.6}Mg_{86.4}$, were obtained by means of μXRF/μXANES. $Rh_{11.0}Mg_{70.0}Al_{19.0}$ was studied after calcination and reduction, while $Rh_{13.6}Mg_{86.4}$ only after the thermal treatment at 900 °C. XRPD failed to determine the distribution of Rh species in the former sample, whereas in the latter Rh-substituted spinels were identified, which makes it possible to compare μXRF/μXRPD and μXRF/μXANES results.

Rh speciation was determined by performing Rh-L3 XANES spot measurements within the Rh layer. In this case, FeCrAlloy foams at different stages were embedded, cut, and polished, and 2D μXRF scans were performed on the obtained cross sections. The Rh, Mg, and Al distributions obtained in this manner stemmed from the (polished) surface in view of their low energy. In Figure 5, the elemental distribution of Mg (red), Fe (green), and Rh (blue) obtained from the $Rh_{11.0}Mg_{70.0}Al_{19.0}$ samples are displayed. On the whole, these elemental distribution maps agree with those obtained by tomographic measurements. The elements of the electrosynthesized coating form a rather homogeneous film which covers the foam struts. Rh distribution maps were used to locate points of interest for speciation (indicated by numbers in Figure 5a, 5b, and 5c). XANES analysis was performed by the linear combination fitting (LCF) using reference spectra (for more details, see the Supporting Information). The results obtained by LCF are in Table S1, while an example of an LCF is shown in Figure 5.

In the calcined $Rh_{11.0}Mg_{70.0}Al_{19.0}$ sample, LCF results indicated that Rh is present not only as part of the spinel phase, as suggested by the correlation of Rh XRF signal and $MgAl_2O_4$ XRPD signal, but also as Rh_2O_3 (presence determined by TPR[10]) and as Rh^0. When no Al was included by electrosynthesis (i.e., $Rh_{13.6}Mg_{86.4}$), XANES measurements confirmed the presence of Rh as spinel and Rh^0 (as identified by XRPD, see Figure 4). The reduction of $Rh_{11.0}Mg_{70.0}Al_{19.0}$ with an equimolar H_2/N_2 gas mixture at 750 °C increased the amount of Rh^0 (state D), but oxidized Rh was still present in $Mg(Rh_xAl_{1-x})_2O_4$ compounds that were more difficult to reduce.

3.2. Catalytic Tests. The catalyst with the largest Rh content, $Rh_{11.0}Mg_{70.0}Al_{19.0}$, was tested in the CPO of CH_4 at an oven temperature of 750 °C and different reaction conditions (Figure 6), i.e. by feeding diluted (CH_4/O_2/He = 2/1/20 v/v)

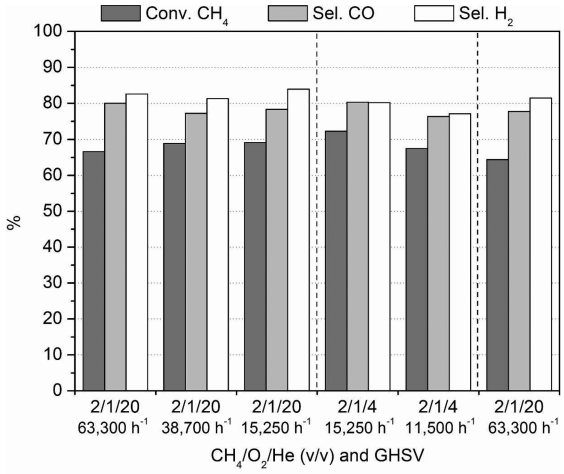

Figure 6. Conversion of methane (Conv. CH_4), selectivity in CO (Sel. CO) and H_2 (Sel. H_2), of $Rh_{11.0}Mg_{70.0}Al_{19.0}$ catalyst at 750 °C oven temperature, by modifying the gas mixture composition (CH_4/O_2/He v/v) and GHSV values.

and concentrated (CH_4/O_2/He = 2/1/4 v/v) gas mixtures; more details can be found elsewhere.[10] When the 2/1/20 v/v gas mixture was fed at 63,300 h^{-1}, increases both in CH_4 conversion from 41 to 66% and in selectivity in CO (from 46 to 80%) and in H_2 (from 48 to 82%) were observed during the first hours of time-on-stream. When the gas mixture was kept constant and the GHSV was decreased, the CH_4 conversion improved. Conversion and selectivity improved by feeding the concentrated gas mixture 2/1/4 v/v and keeping the GHSV constant at 15,250 h^{-1}, while the activity dropped during tests at 11,500 h^{-1}. Moreover, the catalyst steadily deactivated with time-on-stream.

As previously reported,[10] the trend in catalytic performances observed when modifying reaction conditions (GHSV value and CH_4/O_2/He ratio) is related to catalyst features and heat development in the catalytic bed. A small amount of available active sites in the thin catalytic film may explain both the low conversion values reached in all reaction conditions as well as

dx.doi.org/10.1021/cs501079k | ACS Catal. 2014, 4, 3779−3790

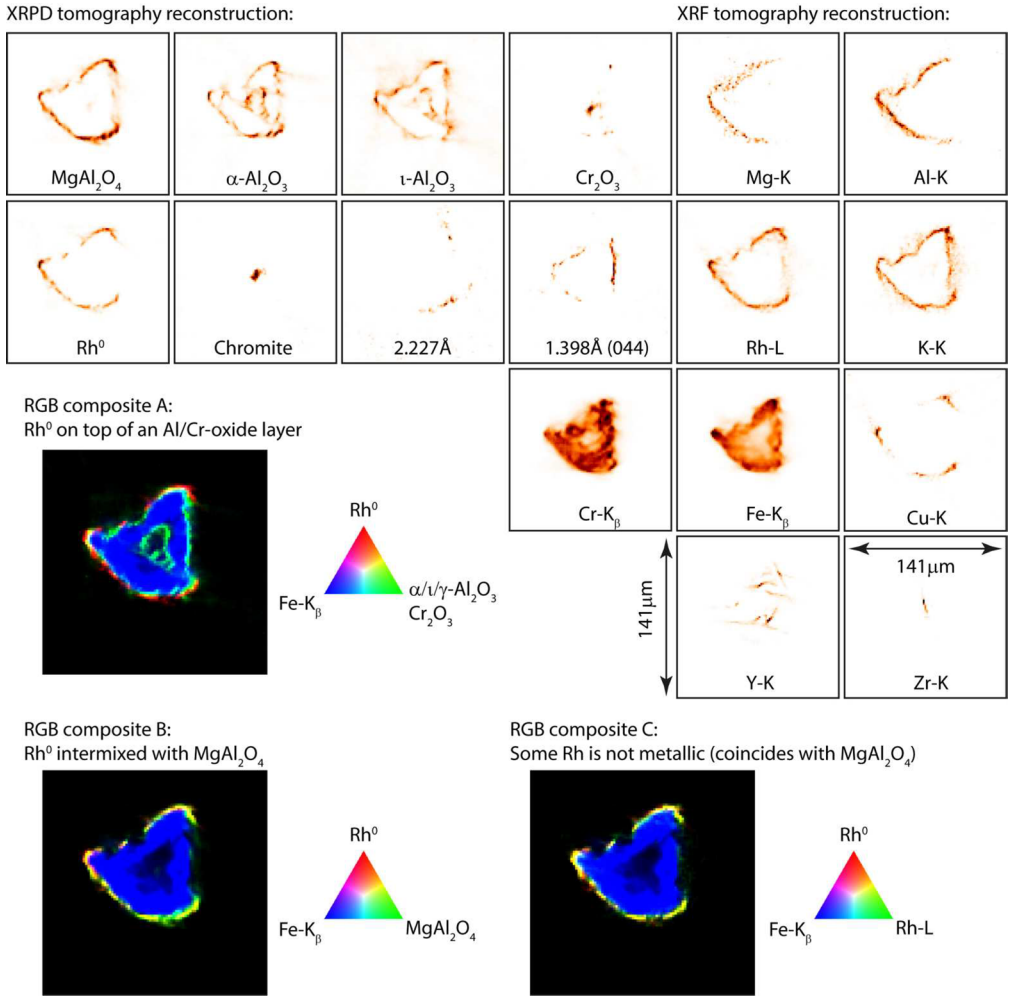

Figure 7. Elemental and crystalline distribution in a virtual cross-section of $Rh_{11.0}Mg_{70.0}Al_{19.0}$ after catalytic tests (state E). Translation: 141 μm (1.5 μm steps); Rotation: 180° (1.5° steps). Time 1 s per point. The unidentified 1.397 Å Bragg peak may be attributed to the most intense reflection (044) of γ-Al_2O_3. RGB composite maps showed that Rh^0 was intermixed with $MgAl_2O_4$ to form a layer on top of an Al/Cr oxide layer that covered the foam surface. Composite C suggested that some rhodium may not be attributed to Rh^0 but rather to $MgAl_2O_4$ (comparison of composites B and C).

the slight increase in activity in tests with the diluted mixture when the GHSV values are decreased. On the other hand, the significant effect of the heat developed by exothermic reactions must be taken into consideration in concentrated tests. The temperature rise in the catalytic bed may promote methane conversion even though the catalyst deactivates with time-on-stream.

From the results reported in this work, it appears that the increase in the catalytic activity during the initial diluted tests may be related to a further activation (reduction) of the catalyst by the reaction gas mixture. In fact, the characterization of the reduced sample confirmed the presence of unreduced Rh^{3+} species. Thus, the formation of spinel rather than MgO by the interaction between coating and metallic support may decrease catalytic performance by decreasing the reducibility of active species.

Lastly, it should be noted that, apart from modifying the catalytic coating during time-on-stream, the temperature increase, presence of oxygen in the first part of the catalytic bed, generation of a reducing environment, and start-up and shut-down cycles may also alter the support itself. Therefore, the foam placed on the top of the catalytic bed was investigated to elucidate these aspects.

3.3. Characterization of Used Catalysts. SEM images of the foam cylinder placed at the top of the catalytic bed confirmed that both the morphology and the thickness of the coating were rather stable under CPO reaction conditions (state E).[10] It should be noted that in this part of the catalytic bed the highest reaction temperatures were reached and the stability of the coating was stressed. The interaction between the metallic foam and the coating may be responsible for this increase in stability. Agglomerates of Rh particles with sizes similar to those in the reduced sample were observed in FEG-SEM images (Figure 1, State D and State E); moreover, smaller (15−40 nm) and more dispersed particles were also identified.

The characterization of the used samples was completed by μXRF/XRPD and μXRF/XANES. Element distributions in a virtual strut cross-section, Figure 7, were quite similar to those in the fresh catalyst, thus further confirming the stability of the coating. The same crystalline phases were identified in $Rh_{11.0}Mg_{70.0}Al_{19.0}$ after CPO tests and calcination (see Figure 2); the only difference between the samples was the presence of Rh^0, which is responsible for the catalytic activity. The coating consisted of a $Rh^0/MgAl_2O_4$ layer on top of an $\alpha/\iota/\gamma$-Al_2O_3/Cr_2O_3 layer. Figure 7 shows that the Rh^0 and XRF Rh-L distributions were correlated in most areas but not everywhere.

dx.doi.org/10.1021/cs501079k | ACS Catal. 2014, 4, 3779−3790

Thus, some of the Rh may be still present as Rh^{3+}. Finally, it should be noted that the FeCrAlloy corrosion did not seem to proceed further during catalytic tests; Al and Cr oxides are stable after catalytic tests (e.g., compare Figure 2 and Figure 7). Despite the fact that oxygen reaches the metallic foam underneath the coating during calcination, thus forming oxidation products, these results show that once the catalyst is formed, the alloy is stable and the catalytic coating-metallic support interaction increases the adhesion and, therefore, the stability of the structured catalyst.

XRF maps obtained in the 2D mode in embedded foams (Figure 5) again confirm that the coating is stable and adherent to the support. The analysis of the corresponding XANES spectra indicated that Rh in the catalyst was further reduced during catalytic tests, i.e. the Rh^0 percentage increased, but some unreduced species were still present, in agreement with XRPD data.

Taking into account the characterization of the samples before and after catalytic tests, it may be stated that the increase in the activity during the first hours of time-on-stream is related to the reduction of leftover Rh^{3+} ions by the reducing gas mixture generated at the high temperatures reached in the catalytic bed. This behavior may also explain the presence of smaller Rh particles in state E instead of state D. On the other hand, the presence of Rh_2O_3 in the used catalyst may be related to the oxidation of metallic particles by feeding the concentrated gas mixture, in agreement with the deactivation observed in catalytic tests. Therefore, XANES results produced information complementary to that obtained by XRPD, which is useful for explaining the catalytic activity.

4. CONCLUSIONS

The interaction between the elements of the catalytic film and the metallic support played a key role in the properties of the Rh catalysts deposited on FeCrAlloy foams; it mainly influenced the nature of crystalline phases and Rh distribution on the catalytic coating as well as the resistance to oxidation of the support alloy. FEG-SEM/EDS provided high spatial resolution information on the morphology of the coating, distribution of the elements, and dispersion of the metallic particles, but only the characterization by microscopic synchrotron techniques such as μXRF/XRPD and μXRF/XANES yielded evidence on the distribution of crystalline phases, oxidation state, and chemical environment of Rh species. As a result of the solid state reaction of electrodeposited Mg and Al with the oxidized Al from the alloy, a spinel phase was always identified by μXRPD, even in the absence of Al in the pristine coating. This interaction had a dual effect: (i) it increased the adhesion of the coating to the support, but (ii) it also reduced the formation of the protective outer alumina shell. Furthermore, the presence of other elements such as K might also promote chromium oxidation. μXANES completed the characterization of the present Rh species with no need for specific requirements regarding their crystallinity. Thus, it was observed that Rh^{3+} cations mainly form a spinel solid solution with Mg after calcination, although some Rh^0 and Rh_2O_3 species were observed. After the reduction pretreatment, only the partial activation of the catalyst took place, since both Rh^{3+} and Rh^0 species were identified. The activation continued during catalytic tests, yielding an increase in the activity at the start of the catalytic tests.

■ ASSOCIATED CONTENT

Supporting Information

Reconstructions of the Fe/Cr alloy bulk material and τ-carbide in a $Rh_{11.0}Mg_{70.0}Al_{19.0}$ strut (Figure S1). Elemental and crystalline distributions in a virtual cross-section of a calcined $Rh_{5.0}Mg_{70.0}Al_{25.0}$ strut (Figure S2). Projected elemental and crystalline distributions in a calcined $Mg_{70.0}Al_{30.0}$ strut (Figure S3). Diffractograms of $Mg(Rh_xAl_{1-x})_2O_4$ and $MgAl_2O_4$ as well as of a mixture of the latter two, which were selected from a tomographic scan of $Rh_{13.6}Mg_{86.4}$ (Figure S4). Projected elemental and crystalline distributions in calcined bare foam strut (Figure S5). Detailed data on the XANES experiment and analysis. This material is available free of charge via the Internet at http://pubs.acs.org.

■ AUTHOR INFORMATION

Corresponding Authors

*Phone: 0039 0512093677. Fax: 0039 0512093679. E-mail: patricia.benito3@unibo.it.

*Phone: 0032 32653326. Fax: 0032 32653233. E-mail: wout.denolf@uantwerpen.be.

Notes

The authors declare no competing financial interest.

■ ACKNOWLEDGMENTS

The authors thank the scientists who assisted during the conducted experiments: D. Grolimund and C. N. Borca for the μXRF/XRPD experiments performed at MicroXAS Beamline of SLS, M. Janousch for the μXRF/XANES experiments at Phoenix Beamline of the SLS, M. Salome for the μXRF/XANES experiments at ID21 Beamline of the ESRF, and I. Guerra for the FEG-SEM/EDS experiments at Granada University. Thanks must go to Porvair for supplying FeCrAlloy foams. The financial support from the Ministero per l'Istruzione, l'Università e la Ricerca (MIUR, Roma, I) is gratefully acknowledged.

■ REFERENCES

(1) Farrauto, R. J.; Liu, Y.; Ruettinger, W.; Ilinich, O.; Shore, L.; Giroux, T. *Catal. Rev.* **2007**, *49*, 141−196.

(2) de Miguel, N.; Manzanedo, J.; Arias, P. L. *Chem. Eng. Technol.* **2012**, *35*, 2195−2203.

(3) Cristiani, C.; Finocchio, E.; Latorrata, S.; Visconti, C. G.; Bianchi, E.; Tronconi, E.; Groppi, G.; Pollesel, P. *Catal. Today* **2012**, *197*, 256−264.

(4) Shamsi, A.; Spivey, J. J. *Ind. Eng. Chem. Res.* **2005**, *44*, 7298−7305.

(5) Cimino, S.; Lisi, L.; Mancino, G.; Musiani, M.; Vázquez-Gómez, L.; Verlato, E. *Int. J. Hydrogen Energy* **2012**, *37*, 1704−17051.

(6) *Structured Catalysts and Reactors*; Cybulski, A., Moulijn, J. A., Eds.; CRC Taylor & Francis: Boca Raton, FL, 2005.

(7) Tronconi, E.; Groppi, G.; Visconti, C. G. *Curr. Opin. Chem. Eng.* **2014**, *5*, 55−67.

(8) Montebelli, A.; Visconti, C. G.; Groppi, G.; Tronconi, E.; Cristiani, C.; Ferreira, C.; Kohler, S. *Catal. Sci. Technol.* **2014**, *4*, 2846−2870.

(9) Basile, F.; Benito, P.; Fornasari, G.; Monti, M.; Scavetta, E.; Tonelli, D.; Vaccari, A. *Catal. Today* **2010**, *157*, 183−190.

(10) Benito, P.; Monti, M.; Bersani, I.; Basile, F.; Fornasari, G.; Scavetta, E.; Tonelli, D.; Vaccari, A. *Catal. Today* **2012**, *197*, 162−169.

(11) Reyero, I.; Velasco, I.; Sanz, O.; Montes, M.; Arzamendia, G.; Gandía, L. M. *Catal. Today* **2013**, *216*, 211−219.

(12) Liu, K.; Deluga, G. D.; Bitsch-Larsen, A.; Schmidt, L. D.; Zhang, L. In *Hydrogen and Syngas Production and Purification Technologies*; Liu,

K., Song, C., Subramani, V., Eds.;John Wiley & Sons, Inc.: Hoboken, NJ, 2010; pp 127−155.
(13) Basini, L. E.; Guarinoni, A. *Ind. Eng. Chem. Res.* **2013**, *52*, 17023−17037.
(14) Bortolozzi, J. P.; Banús, E. D.; Milt, V. G.; Gutierrez, L. B.; Ulla, M. A. *Appl. Surf. Sci.* **2010**, *257*, 495−502.
(15) Quadakkers, W. J.; Bennett, M. J. *Mater. Sci. Technol.* **1994**, *10*, 126−131.
(16) Amano, T.; Takezawa, Y.; Shiino, A.; Shishido, T. *J. Alloys Compd.* **2008**, *452*, 16−22.
(17) Badini, C.; Laurella, F. *Surf. Coat. Technol.* **2001**, *135*, 291−298.
(18) Golightly, F. A.; Wood, G. C.; Stott, F. H. *Oxid. Met.* **1980**, *14*, 217−234.
(19) Zhu, C.; Zhao, X.; Molchan, I. S.; Thompson, G. E.; Liang, G.; Xiao, P. *Mater. Sci. Eng., A* **2011**, *528*, 8687−8693.
(20) Yang, Z.; Xia, G.-G.; Walker, M. S.; Wang, C.-M.; Stevenson, J. W.; Singh, P. *Int. J. Hydrogen Energy* **2007**, *32*, 3770−3777.
(21) Quadakkers, W. J.; Naumenko, D.; Wessel, E.; Kochubey, V.; Singheiser, L. *Oxid. Met.* **2004**, *61*, 17−37.
(22) Graham, M. J.; Hussey, R. J. *Corros. Sci.* **2002**, *44*, 319−330.
(23) Kaltner, W.; Veprek-Heijman, M.; Jentys, A.; Lercher, J. A. *Appl. Catal., B* **2009**, *89*, 123−127.
(24) Martínez, T. L. M.; Sanz, O.; Centeno, M. A.; Odriozola, J. A. *Chem. Eng. J.* **2010**, *162*, 1082−1090.
(25) Giornelli, T.; Löfberg, A.; Guillou, L.; Paul, S.; Le Courtois, V.; Bordes-Richard, E. *Catal. Today* **2007**, *128*, 201−207.
(26) Zamaro, J. M.; Ulla, M. A.; Miró, E. E. *Microporous Mesoporous Mater.* **2008**, *115*, 113−122.
(27) Milt, V. G.; Ivanova, S.; Sanz, O.; Domínguez, M. I.; Corrales, A.; Odriozola, J. A.; Centeno, M. A. *Appl. Surf. Sci.* **2013**, *270*, 169−177.
(28) Martínez Tejada, L. M.; Domínguez, M. I.; Sanz, O.; Centeno, M. A.; Odriozola, J. A. *Gold Bull.* **2013**, *46*, 221−231.
(29) Domínguez, M. I.; Pérez, A.; Centeno, M. A.; Odriozola, J. A. *Appl. Catal., A* **2014**, *478*, 45−57.
(30) Basile, F.; Fornasari, G.; Rosetti, V.; Trifirò, F.; Vaccari, A. *Catal. Today* **2004**, *91*−*92*, 293−297.
(31) Basile, F.; Benito, P.; Fornasari, G.; Vaccari, A. *Appl. Clay Sci.* **2010**, *48*, 250−259.
(32) Hernández-Garrido, J. C.; Gómez, D. M.; Gaona, D.; Vidal, H.; Gatica, J. M.; Sanz, O.; Rebled, J. M.; Peiró, F.; Calvino, J. J. *J. Phys. Chem. C* **2013**, *117*, 13028−13036.
(33) Cimino, S.; Gerbasi, R.; Lisi, L.; Mancino, G.; Musiani, M.; Vázquez-Gómez, L.; Verlato, E. *Chem. Eng. J.* **2013**, *230*, 422−431.
(34) Basile, F.; Benito, P.; Bugani, S.; De Nolf, W.; Fornasari, G.; Janssens, K.; Morselli, L.; Scavetta, E.; Tonelli, D.; Vaccari, A. *Adv. Funct. Mater.* **2010**, *20*, 4117−4126.
(35) Janssens, K.; Alfeld, M.; Van der Snickt, G.; De Nolf, W.; Vanmeert, F.; Radepont, M.; Monico, L.; Dik, J.; Cotte, M.; Falkenberg, G.; Miliani, C.; Brunetti, B. G. *Annu. Rev. Anal. Chem.* **2013**, *6*, 399−425.
(36) Espinosa-Alonso, L.; O'Brien, M. G.; Jacques, S. D. M.; Beale, A. M.; de Jong, K. P.; Barnes, P.; Weckhuysen, B. M. *J. Am. Chem. Soc.* **2009**, *131*, 16932−16938.
(37) Beale, A. M.; Jacques, S. D. M.; Weckhuysen, B. M. *Chem. Soc. Rev.* **2010**, *39*, 4656−4672.
(38) Ristanović, Z.; Hofmann, J. P.; Deka, U.; Schlli, T. U.; Rohnke, M.; Beale, A. M.; Weckhuysen, B. M. *Angew. Chem., Int. Ed.* **2013**, *52*, 13382−13386.
(39) Ruiz-Martinez, J.; Beale, A. M.; Deka, U.; O'Brien, M. G.; Quinn, P. D.; Mosselmans, J. F. W.; Weckhuysen, B. M. *Angew. Chem., Int. Ed.* **2013**, *52*, 5983−5987.
(40) Beale, A. M.; Gibson, E. K.; O'Brien, M. G.; Jacques, S. D. M.; Cernik, R. J.; Di Michiel, M.; Cobden, P. D.; Pirgon-Galin, Ö.; van de Water, L.; Watson, M. J.; Weckhuysen, B. M. *J. Catal.* **2014**, *314*, 94−100.
(41) Janssens, K.; De Nolf, W.; Van Der Snickt, G.; Vincze, L.; Vekemans, B.; Terzano, R.; Brenker, F. E. *Trends Anal. Chem.* **2010**, *29*, 464−478.
(42) Van der Snickt, G.; Janssens, K.; Dik, J.; De Nolf, W.; Vanmeert, F.; Jaroszewicz, J.; Cotte, M.; Falkenberg, G.; Van der Loeff, L. *Anal. Chem.* **2012**, *84*, 10221−10228.
(43) Mino, L.; Borfecchia, E.; Groppo, C.; Castelli, D.; Martinez-Criado, G.; Spiesse, R.; Lamberti, C. *Catal. Today* **2014**, *229*, 72−79.
(44) Nagaoka, K.; Jentys, A.; Lercher, J. A. *J. Catal.* **2005**, *229*, 185−196.
(45) Grunwaldt, J.-D.; Hannemann, S.; Schroer, C. G.; Baiker, A. *J. Phys. Chem. B* **2006**, *110*, 8674−8680.
(46) Hannemann, S.; Grunwaldt, J.-D.; van Vegten, N.; Baiker, A.; Boye, P.; Schroer, C. G. *Catal. Today* **2007**, *126*, 54−63.
(47) Kimmerle, B.; Haider, P.; Grunwaldt, J.-D.; Baiker, A.; Boye, P.; Schroer, C. G. *Appl. Catal., A* **2009**, *353*, 36−45.
(48) Bertrand, L.; Robinet, L.; Thoury, M.; Janssens, K.; Cohen, S. X.; Schöder, S. *Appl. Phys. A: Mater. Sci. Process.* **2012**, *106*, 377−396.
(49) Sham, T. K. *Phys. Rev. B* **1985**, *31*, 1888−1902.
(50) Wu, Y.; Ellis, D. E. *J. Phys.: Condens. Matter* **1995**, *7*, 3973−3989.
(51) Shimizu, K.-i.; Oda, T.; Sakamoto, Y.; Kamiya, Y.; Yoshida, H.; Satsuma, A. *Appl. Catal., B* **2012**, *111*−*112*, 509−514.
(52) Borca, C. N.; Grolimund, D.; Willimann, M.; Meyer, B.; Jefimovs, K.; Vila-Comamala, J.; David, C. *J. Physics: Conference Series* **2009**, *186*, No. 012003.
(53) De Nolf, W.; Janssens, K. *Surf. Interface Anal.* **2010**, *42*, 411−418.
(54) De Nolf, W. Ph.D. Thesis, University of Antwerp, Belgium, 2013. http://dx.doi.org/10067/1109100151162165141 (accessed July 29, 2014).
(55) De Nolf, W.; Vanmeert, F.; Janssens, K. *J. Appl. Crystallogr.* **2014**, *47*, 1107−1117.
(56) Vekemans, B.; Janssens, K.; Vincze, L.; Adams, F.; Van Espen, P. *X-Ray Spectrom.* **1994**, *23*, 278−285.
(57) http://xrdua.ua.ac.be/ (accessed July 29, 2014).
(58) McMaster, W. H.; Kerr Del Grande, N.; Mallett, J. H.; Hubbell J. H. *Compilation of X-ray Cross Sections*; Lawrence Radiation Laboratory UCRL-50174 sec II, Rev. 1, 1969.
(59) Ravel, B.; Newville, M. *J. Synchrotron Radiat.* **2005**, *12*, 537−541.
(60) Nguyen, B. N. T.; Leclerc, C. A. *J. Power Sources* **2007**, *163*, 623−629.
(61) Hou, P. Y. *Mater. Corros.* **2000**, *51*, 329−337.
(62) Kochubey, V.; Naumenko, D.; Wessel, E.; Le Coze, J.; Singheiser, L.; Al-Badairy, H.; Tatlock, G. J.; Quadakkers, W. J. *Mater. Lett.* **2006**, *60*, 1654−1658.
(63) Foster, P. A. *J. Am. Ceram. Soc.* **1960**, *43*, 66−68.
(64) Fischer, R. X.; Schmücker, M.; Angerer, P.; Schneider, H. *Am. Mineral.* **2001**, *86*, 1513−1518.
(65) Kucharík, M.; Korenko, M.; Janičkovič, D.; Kadlečíková, M.; Boča, M.; Obona, J. V. *Monatsh. Chem.* **2010**, *141*, 7−13.
(66) Smrčok, L.; Langer, V.; Křestan, J. *Acta Crystallogr.* **2006**, *C62*, i83−i84.
(67) Chegroune, R.; Salhi, E.; Crisci, A.; Wouters, Y.; Galerie, A. *Oxid. Met.* **2008**, *70*, 331−337.
(68) Petterson, J.; Svensson, J.; Johansson, L.-G. *Mater. Sci. Forum* **2008**, *595*−*598*, 367−375.
(69) Lehmusto, J.; Lindberg, D.; Yrjas, P.; Skrifvars, B.-J.; Hupa, M. *Corros. Sci.* **2012**, *59*, 55−62.
(70) Li, Y. S.; Niu, Y.; Spiegel, M. *Corros. Sci.* **2007**, *49*, 1799−1815.
(71) Basile, F.; Fornasari, G.; Gazzano, M.; Vaccari, A. *J. Mater. Chem.* **2002**, *12*, 3296−3303.
(72) Andreozzi, G. B.; Princivalle, F.; Skogby, H.; Della Giusta, A. *Am. Mineral.* **2000**, *85*, 1164−1171.
(73) Capobianco, C. J. *Thermochim. Acta* **1993**, *220*, 7−16.
(74) Agrafiotis, C.; Tsetsekou, A. *J. Eur. Ceram. Soc.* **2000**, *20*, 815−824.
(75) Agüero, A.; Gutiérrez, M.; Korcakova, L.; Nguyen, T. T. M.; Hinnemann, B.; Saadi, S. *Oxid. Met.* **2011**, *76*, 23−42.